

Cover Page



Universiteit Leiden



The handle <http://hdl.handle.net/1887/138639> holds various files of this Leiden University dissertation.

Author: Mandal, S.

Title: Revealing the nature of new low-frequency radio source populations

Issue Date: 2020-12-10

Chapter 4

Towards a sample of radio phoenices in galaxy clusters

Based on
S. Mandal, R. J. van Weeren, T. W. Shimwell, H. T. Intema, A. Botteon,
F. de Gasperin, G. Di Gennaro, M. Grespan, G. Brunetti, M. Brüggen,
M. Brienza, F. Gastaldello, M. J. Hardcastle, H. Röttgering, R. Kraft,
R. Cassano, A. Drabent, M. Hoeft, D. Jung, L. K. Morabito, A. Shulevski,
W. L. Williams et al. Submitted to A&A

Abstract

Over the last decade, it has been well established that shocks and turbulent motions in the intra-cluster medium (ICM) generated through cluster mergers can produce observable large scale synchrotron emission. However, the related particle acceleration mechanisms responsible for these phenomena are still not clearly understood. In addition, the complexity of objects observed has put the traditional taxonomy of diffuse radio sources as consisting of radio halos and radio relics into question. In order to explain the acceleration efficiencies for radio relics and radio halos, the presence of fossil plasma has been suggested. Old lobes of radio galaxies are one of the key candidates for the source of these mildly relativistic particles. Typically these lobes have an ultra-steep spectrum because the high-energy radio emitting electrons would have lost their energy due to synchrotron and inverse Compton (IC) losses. However, with plasma instabilities driven by complex cluster dynamics and their interplay with the ICM that can re-energise old fossil electrons to emit observable radio waves again, these sources of emission are known as radio phoenixes. In this paper we present an observational overview of all the known radio phoenixes. Out of 25 sources that are presented, 8 are discoveries that we present here and for these we show results from new radio (GMRT and/or LOFAR) and, for a subset, X-ray observations. The sample allows us to study the common physical properties of radio phoenixes (such as radio morphology, dynamical state of the host cluster, location of the phoenixes inside the cluster and spectral behaviour) to establish the nature of this relatively unexplored class of objects. These radio phoenixes are found to have an AGN origin and are located well within the R_{500} of the clusters. Presence of dynamical disturbance in the cluster supports the formalism that they are associated with ICM motion and or shocks. Finally, while these revived fossil plasma sources are found to have a curved spectra at higher frequencies, presence of non-uniform spectral indices suggests that they should not be thought to represent a reservoir of uniform cosmic-ray population.

4.1 Introduction

Clusters of galaxies are the grow via the accretion of smaller groups of galaxies and through major mergers with other clusters of galaxies. Galaxy cluster mergers release a huge amount ($10^{63} - 10^{64}$ ergs) of energy into the Intra-cluster medium (ICM) (e.g. [Kravtsov & Borgani 2012](#)). This released binding energy strongly affects the physical properties of the ICM ([Markevitch & Vikhlinin](#)

2007). In addition, a fraction of energy can be channeled into non-thermal components, relativistic particles and magnetic fields, that produce observable synchrotron emission on cluster scale (Brunetti & Jones 2014). The synchrotron emission has a steep spectra ($S \propto \nu^\alpha$; where α is the spectral index, S is the total flux density and ν is the observed frequency) and is observed in the form of radio halos, radio relics etc. (van Weeren et al. 2019).

Radio halos are extended (~ 1 Mpc) diffuse radio sources which has a morphology and centroid that roughly matches the X-ray emission from the thermal ICM (e.g. Cassano et al. 2010, Kale et al. 2015, Cuciti et al. 2015). The most favoured scenario suggests that radio halos are formed by continuous (re)-acceleration of electrons due to turbulence generated from cluster mergers (Brunetti et al. 2001, Petrosian 2001, Brunetti & Lazarian 2007, Brunetti & Lazarian 2011, Miniati & Beresnyak 2015, Brunetti & Lazarian 2016, Pinzke et al. 2017). Recently it has been proposed by Brügggen & Vazza (2020) that these mechanisms may also be responsible for radio bridges between clusters (Botteon et al. 2018b, Govoni et al. 2019).

Radio relics are linearly polarised (10% to 30% at GHz frequencies) and have an elongated morphology. They are located at the outskirts of merging clusters and are thought to trace shock waves (Ensslin et al. 1998, van Weeren et al. 2010, Finoguenov et al. 2010, Bonafede et al. 2012, Bourdin et al. 2013, Akamatsu & Kawahara 2013, Stroe et al. 2013, de Gasperin et al. 2015, Shimwell et al. 2015, Botteon et al. 2016, Urdampilleta et al. 2018 etc). Diffusive shock acceleration (DSA: a Fermi I mechanism) had primarily been proposed to be responsible for the non-thermal energy gain of the particles at shock fronts (Ensslin et al. 1998, Roettiger et al. 1999). However, recent observations have put this framework into question. In a fraction of cases, it has been shown that the acceleration efficiency is not high enough to generate such bright radio relics with electrons from the thermal pool (e.g. Botteon et al. 2016, Eckert et al. 2016, van Weeren et al. 2016a, Botteon et al. 2019). In this regard, the role of seed particles (fossil plasma) in the ICM has been invoked, since re-acceleration of seed electrons is more efficient than that the DSA (Markevitch et al. 2002, Kang et al. 2012, Kang & Ryu 2015).

Radio phoenixes are a less widely studied class of objects that are thought to be a manifestation of fossil plasma in the ICM (Kempner et al. 2004, van Weeren et al. 2019). Lobes and tails of radio galaxies in clusters are likely candidates for these fossil electrons. When the central AGN of a radio galaxy switches off and there is no supply of freshly injected particles, the so-called ‘AGN remnant lobes’ can diffuse into the surrounding medium. After being deposited in the ICM, electrons from these lobes are only visible for tens of

Myrs at higher (\sim GHz) frequencies. Due to adiabatic and radiative losses, their spectrum becomes steep ($\alpha \leq -1.2$) and curved. The fossil plasma becomes invisible and hard to detect, even at sub GHz frequencies (Brienza et al. 2017, Hardcastle 2018, English et al. 2019). However, in a cluster environment, these low-energy relativistic ($\gamma \sim 100$) electrons can still be poorly mixed with the ICM (Sarazin 1999; Petrosian 2001; Pinzke et al. 2013).

When (weak) shocks generated from cluster mergers pass through these old radio lobes, they can adiabatically compress and re-energize the electrons, thereby boosting their visibility at lower-radio (hundreds of MHz) frequencies (Enßlin & Gopal-Krishna 2001, Enßlin & Brüggen 2002). Thus these revived fossil plasma sources provide us with a unique opportunity to study this otherwise invisible populations of electrons. Although these fossil electrons are deposited locally, over time, due to advection and turbulent diffusion, they can occupy a large fraction of ICM. Therefore, old radio lobes could provide a seed population of relativistic electrons and a possible connection between radio galaxies and re-acceleration mechanisms in both radio halos and relics. For example, de Gasperin et al. (2017) showed evidence of an interplay between fossil radio plasma and the perturbed ICM which appeared to gently re-accelerate relativistic particles injected by an AGN. Also, it has been shown that shocks generated through cluster mergers can power radio relic type sources by re-accelerating electrons of AGN origin (van Weeren et al. 2017). However, the relative importance of these mechanisms to explain the diffuse radio sources, is not fully understood and to date, only few radio phoenixes have been discovered (Slee et al. 2001, Kempner et al. 2004, van Weeren et al. 2009, van Weeren et al. 2011, de Gasperin et al. 2015, Di Gennaro et al. 2018, Mandal et al. 2020). In order to understand the acceleration mechanisms responsible for the generation of radio phoenixes, it is crucial to identify their common observational and physical properties and compare them with those of radio halos and relics. This will also help in establishing radio phoenixes as a distinct class of objects and enable us in better understanding of the physics of particle acceleration and the nature of this relatively unexplored population. Even though fossil electrons from radio lobes in clusters of galaxies are abundant, their ultra-steep nature makes them hard to be identify at high (GHz) frequencies. Due to the ultra-steep spectral nature of these sources, large area surveys at low frequencies (\sim below 300 MHz) are ideal to look for radio phoenixes. One promising example, is the TIFR GMRT Sky Survey (TGSS ADR; Intema et al. 2017) which is a $25''$ resolution sky survey at 150 MHz which covers the radio sky between -53° to $+90^\circ$ (approximately 90%) with a sensitivity of $2\text{-}5\text{mJy beam}^{-1}$ rms noise.

As part of a pilot study, we discovered 11 new radio phoenix candidates.

In [Mandal et al. \(2020\)](#), we presented detailed follow-up (radio and X-ray) observations for three of these sources. In this paper, we present the results from the follow-up observations for the other 8 sources, for one of which, polarisation results are also included. In addition, we extend our sample of radio phoenixes by including all the previously known candidates we are aware of in the literature (see Section 4.2 for details) and use this larger sample to investigate the global physical properties of this class of sources.

The layout of the paper is as follows. In Section 4.2 we describe the method of sample selection, that we used to identify candidate radio phoenixes. This is followed by observation and data reduction methods in Section 4.3. In Section 4.4 we present the results deduced from the whole sample of radio phoenixes (new discoveries and previously known sources) and discussed the possible common properties of this sample in Section 4.5. This is followed by discussions and possible interpretations described in Section 4.6 and conclusions in Section 4.7.

Throughout the paper we assume a Λ CDM cosmology with $H_0 = 70$ $\text{kms}^{-1}\text{Mpc}^{-1}$, $\Omega_m = 0.3$, and $\Omega_\Lambda = 0.7$. All sky coordinates are epoch J2000 coordinates. This paper makes use of the cosmology calculator ([Wright 2006](#)) to compute cosmological parameters.

Table 4.1: List of all radio phoenix candidates (known to date) along with their properties.

Cluster name / Target	RA (J2000)	Dec (J2000)	Redshift (z)	Conversion (kpc/arcsec)	Reference ^a
Abell 1914	14 ^h 26 ^m 01.6 ^s	+37°49'38"	0.171	2.914	1
SDSS-C4-DR3-3088	09 ^h 46 ^m 45.4 ^s	+54°25'37"	0.046	0.904	2
Abell 2593	23 ^h 24 ^m 20.2 ^s	+14°39'04"	0.041	0.810	2
Abell 2048	15 ^h 15 ^m 17.8 ^s	+04°22'56"	0.097	1.796	2,7
Abell 1033	10 ^h 31 ^m 33.7 ^s	+35°04'34"	0.126	2.257	3
Abell 2443	22 ^h 26 ^m 02.6 ^s	+17°22'41"	0.108	1.975	4,18
Abell 133	01 ^h 02 ^m 42.1 ^s	-21°52'25"	0.057	1.105	5,17
Abell 85	00 ^h 41 ^m 50.1 ^s	-09°18'07"	0.055	1.069	5,6
24P73	22 ^h 17 ^m 36.2 ^s	+59°44'07"	0.15	2.616	7
Ophiuchus	17 ^h 12 ^m 26.0 ^s	-23°22'33"	0.028	0.562	8,9
Abell 2256	17 ^h 03 ^m 43.5 ^s	+78°43'03"	0.058	1.123	10
Abell 1931	14 ^h 31 ^m 59.7 ^s	+44°15'48"	0.17	2.898	11
MaxBCG J217.95869+13.53470	14 ^h 31 ^m 50.1 ^s	+13°32'05"	0.16	2.758	12,13
Abell 725	09 ^h 01 ^m 11.6 ^s	+62°36'14"	0.090	1.680	14
Abell 4038	23 ^h 47 ^m 43.2 ^s	-28°08'29"	0.028	0.562	15
Abell 13	00 ^h 13 ^m 38.3 ^s	-19°30'08"	0.094	1.746	5
Abell S753	14 ^h 03 ^m 35.9 ^s	-33°59'16"	0.014	0.286	16
CIZA J1926.1+4833	19 ^h 26 ^m 10.6 ^s	+48°32'44"	0.098	1.812	this work
MKW8	14 ^h 40 ^m 38.2 ^s	+03°28'35"	0.027	0.543	"
Abell 565	07 ^h 07 ^m 24.8 ^s	+71°45'22"	0.105	1.925	"
Abell 2675	23 ^h 55 ^m 33.4 ^s	+11°25'42"	0.071	1.354	"
Abell 272	01 ^h 55 ^m 19.1 ^s	+33°56'41"	0.088	1.646	"
Abell 566	07 ^h 04 ^m 24.5 ^s	+63°18'58"	0.097	1.795	"
Abell 2751	00 ^h 16 ^m 19.8 ^s	-31°21'55"	0.107	1.958	"
Abell 661	08 ^h 27 ^m 15.7 ^s	+53°08'06"	0.12	2.164	"

^a 1: Mandal et al. (2019), 2: Mandal et al. (2020), 3: de Gasperin et al. (2015), 4: Clarke et al. (2013), 5: Slee et al. (2001), 6: Durret et al. (2005), 7: van Weeren et al. (2009), 8: Werner et al. (2016), 9: Murgia et al. (2010), 10: van Weeren et al. (2012b), 11: Brüngen et al. (2018), 12: O'grean et al. (2011), 13: Shulevski et al. (2015), 14: Kempner & Sarazin (2001), 15: Kale et al. (2018), 16: Subrahmanyan et al. (2003), 17: Randall et al. (2010), 18: Cohen & Clarke (2011)

Table 4.2: Observation details of the radio phoenixes that are presented in this paper. ROSAT All-Sky Survey data have been used for the sources that do not have *Chandra* or *XMM-Newton* data.

Source ^a	LOFAR 150 MHz (120-168)MHz	GMRT 325 MHz (308-340)MHz	GMRT 610 MHz (594-626)MHz	<i>Chandra</i>	<i>XMM-Newton</i>
Abell 1914	8.33 h	3.83 h	3.18 h	✓	-
SDSS-C4-DR3-3088	8.33 h	3.68 h	3.55 h	✓	-
Abell 2593	8.33 h	3.83 h	3.18 h	✓	-
Abell 2048	8.33 h	10 h	10 h	-	✓
Abell 1033	8.33 h	4.85 h	-	✓	-
Abell 2443	8.33 h	-	-	-	✓
Abell 133	-	5.21 h	-	-	✓
Abell 85	-	4.11 h	-	-	✓
24P73	-	9.66 h	7.7 h	✓	-
Ophiuchus	-	-	6.0 h	-	✓
Abell 2256	-	-	6.6 h	✓	-
Abell 1931	-	-	-	✓	-
MaxBCG J217.95869+13.53470	-	9.16 h	-	✓	-
Abell 725	8.33 h	-	-	-	-
Abell 4038	-	5.35 h	-	-	✓
CIZA J1926.1+4833	-	3.75 h	3.23 h	-	✓
MKW8	8.33 h	7.06 h	8.33 h	-	✓
Abell 565	-	3.68 h	-	-	✓
Abell 2675	-	3.33 h	-	-	✓
Abell 272	8.33 h	6.23 h	-	-	✓
Abell 566	-	4.83 h	-	-	-
Abell 2751	-	3.71 h	3.81 h	-	-
Abell 661	-	4.18 h	3.73 h	-	-

^a Abell 13 and Abell S753 lack legacy GMRT or LOFAR data and we do not show any radio images for these two sources. Therefore, these two sources are not in this list.

Table 4.3: Mass, radio power at 325 MHz and dynamical state of the host clusters for the sample of radio phoenixes.

Cluster name / Target	Mass ^a (M_{500}) ($\times 10^{14} M_{\odot}$)	Radio Power (P_{325}) ($\times 10^{24}$ W/Hz)	Radius (R_{500}) ^b (kpc)	Dynamical state
Abell 1914 ⁽¹⁾	$7.24^{+0.26}_{-0.26}$	81.0 ± 8.0	1294 ± 15	Un-relaxed
SDSS-C4-DR3-3088 ⁽²⁾	$1.69^{+0.39}_{-0.39}$	2.34 ± 0.26	828 ± 61	Un-relaxed
Abell 2593 ⁽¹⁾	$1.82^{+0.17}_{-0.18}$	5.80 ± 0.60	1011 ± 27	Un-relaxed
Abell 2048 ⁽²⁾	$2.97^{+0.11}_{-0.11}$	14.3 ± 1.4	983 ± 12	Un-relaxed
Abell 1033 ⁽¹⁾	$3.24^{+0.30}_{-0.32}$	17.8 ± 1.9	1037 ± 32	Un-relaxed
Abell 2443 ⁽¹⁾	$3.77^{+0.26}_{-0.27}$	13.4 ± 0.70	1060 ± 25	Un-relaxed
Abell 133 ⁽¹⁾	$3.01^{+0.18}_{-0.16}$	34.3 ± 3.4	1000 ± 19	Un-relaxed
Abell 85 ⁽¹⁾	$4.91^{+0.12}_{-0.17}$	21.7 ± 2.2	1178 ± 12	Un-relaxed
24P73	—	29.0 ± 2.8	—	Un-relaxed
Ophiuchus ⁽³⁾	5.31	12.0 ± 1.2	1219	Un-relaxed
Abell 2256 ⁽¹⁾	$6.21^{+0.10}_{-0.09}$	2.81 ± 0.28	1122 ± 7	Un-relaxed
Abell 1931 ⁽⁴⁾	$1.62^{+2.04}_{-0.72}$	0.27 ± 0.58	784 ± 58	Un-relaxed
MaxBCG: J217.95869+13.53470 ⁽³⁾	1.00	4.8 ± 0.5	670	Un-relaxed
Abell 725 ⁽³⁾	3.20	7.94 ± 0.9	1010	N/A
Abell 4038 ⁽¹⁾	$1.48^{+0.11}_{-0.10}$	2.66 ± 0.27	796 ± 19	Un-relaxed
Abell 13 ⁽¹⁾	$2.75^{+0.23}_{-0.24}$	15.3 ± 1.5	981 ± 28	Un-relaxed
Abell S753 ⁽³⁾	0.26	3.80 ± 0.4	448	N/A
CIZA J1926.1+4833 ⁽¹⁾	$3.09^{+0.19}_{-0.22}$	8.77 ± 0.9	995 ± 22	Un-relaxed
MKW8 ⁽¹⁾	$1.10^{+0.18}_{-0.20}$	0.43 ± 0.04	722 ± 42	Un-relaxed
Abell 565 ⁽³⁾	1.62	3.11 ± 0.31	801	N/A
Abell 2675 ⁽¹⁾	$2.39^{+0.25}_{-0.23}$	1.32 ± 0.13	922 ± 31	Un-relaxed
Abell 272 ⁽³⁾	2.83	4.43 ± 0.40	970	Un-relaxed
Abell 566 ⁽¹⁾	$2.94^{+0.24}_{-0.27}$	40 ± 4.0	979 ± 28	N/A
Abell 2751 ⁽³⁾	1.26	56.0 ± 6.0	736	N/A
Abell 661	—	296 ± 30	—	N/A

^a The M_{500} values are taken from (1) Planck Catalogue (Planck Collaboration et al. 2016), (2) Scaling relations from Arnaud et al. (2005), (3) MCXC Catalogue (Piffaretti et al. 2011) and (4) Brüngen et al. (2018)

^b $R_{500} = \sqrt[3]{\frac{3M_{500}}{4\pi(500\rho_c)}}$, where ρ_c is the critical density of the Universe at the given redshift.

Table 4.4: Largest linear scales, distances from the cluster centre and integrated spectral indices for the sample of radio phenices. Note that, for the calculation of the largest linear scales, we have used the radio images at the lowest available frequencies. See Table 4.2 for the summary of radio and X-ray data.

Cluster name / Target	LLS (kpc)	Dist (kpc)	Spectra Index 1 ($\alpha_{150-325}$)	Spectral Index 2 ($\alpha_{325-1400}$)
Abell 1914	492	189	-2.23 ± 0.18	-2.17 ± 0.07
SDSS-C4-DR3-3088	300	349	-1.81 ± 0.19	-2.09 ± 0.10
Abell 2593	432	76	-2.16 ± 0.18	-1.10 ± 0.07
Abell 2048	360	260	-1.35 ± 0.25	-2.30 ± 0.17
Abell 1033	304	76	-1.34 ± 0.14	-1.58 ± 0.07
Abell 2443	541	50	-2.83 ± 0.26	-2.84 ± 0.16
Abell 133	425	283	-1.24 ± 0.19	-2.05 ± 0.10
Abell 85	290	438	-1.38 ± 0.17	-2.89 ± 0.09
24P73	339	117	-1.58 ± 0.13	-2.41 ± 0.18
Ophiuchus	140	200	-1.16 ± 0.09	-0.97 ± 0.04
Abell 2256	274	238	-0.66 ± 0.18	-1.94 ± 0.07
Abell 1931	520	230	-3.01 ± 0.38	-1.37 ± 1.32
MaxBCG J217.95869+13.53470	124	165	-1.09 ± 0.23	-2.80 ± 0.12
Abell 725	372	221	-0.85 ± 0.19	-0.86 ± 0.08
Abell 4038	54	20	-1.45 ± 0.20	-2.15 ± 0.08
Abell 13	260	200	-1.92 ± 0.34	-2.08 ± 0.12
Abell S753	–	–	-1.44 ± 0.0	-1.99 ± 0.0
CIZAJ1926.1+4833	496	207	-1.61 ± 0.11	-2.33 ± 0.11
MKW8	120	50	-1.84 ± 0.19	-3.23 ± 0.10
Abell 565	348	47	-1.28 ± 0.19	-2.05 ± 0.08
Abell 2675	173	71	-1.23 ± 0.20	-1.72 ± 0.08
Abell 272	291	208	-1.64 ± 0.18	-2.43 ± 0.07
Abell 566	270	63	-1.88 ± 0.21	-2.32 ± 0.09
Abell 2751	454	368	-0.77 ± 0.20	-1.34 ± 0.09
Abell 661	361	587	-0.62 ± 0.20	-1.06 ± 0.08

4.2 Sample Selection

One of the key observational properties of radio phoenixes is their ultra-steep nature. Therefore, we used the 150 MHz TGSS (resolution: $25''$) and convolved it to the resolution of 1.4 GHz NRAO VLA Sky Survey (NVSS; Condon et al. 1998: resolution $45''$) and combined the two, to look for ultra-steep spectrum sources. We selected bright (see below) sources that have a spectral index (α) ≤ -2 . The value of the spectral index in the selection of sources is somewhat arbitrary, but was necessary to limit the sample size for follow-up observations. The ultra-steep spectral index in combination with the sensitivity limit also minimise the possibility of a source being a radio halo or relic which typically have spectral indices of -1.3 to -1.1 (van Weeren et al. 2019). In addition, we also imposed the following criteria:

- A 150 MHz TGSS total flux density $S_{150} > 30$ mJy (10σ detection);
- located in the vicinity of a known cluster position (within ~ 1 Mpc) from the SDSS cluster catalogue (Wen et al. 2012) or the ROSAT All-Sky Survey (RASS: Voges et al. 1999) data;
- A morphology compatible with extended cluster emission

This sample of objects with an ultra-steep spectrum nature and extended morphology is likely the tip of the iceberg of the population. Our search also yielded ultra-steep spectrum objects that included previously known radio phoenixes and a serendipitous detection of Jupiter.¹ Our final sample consisted of 11 revived fossil plasma sources which are new discoveries and three of which were previously followed up. For this sample, we obtained deeper data at different radio frequencies with GMRT and/or LOFAR. Note that, previously known radio phoenixes were not re-observed. For three of the objects (Abell 2593, SDSS-C4-DR3-3088 and 24P73), we also obtained pointed X-ray data. In Mandal et al. (2020), we presented a detailed study of three of these revived fossil plasma sources. To extend our sample of radio phoenixes we inspected all the sources that are classified as ‘revived fossil plasma sources’ (referred as ‘F’ in the very recent review by van Weeren et al. 2019). If these sources have a filamentary morphology, appear to be resolved and have a steep spectra ($\alpha \leq -1$; with a hint of a curvature towards high-frequency), we consider them in our sample of radio

¹One of the target sources was not detected in follow-up observations. Closer inspection of the TGSS observational details revealed that this was a chance-alignment of Jupiter moving in front of a galaxy cluster.

phoenices. This yielded a list of 25 sources including the new discoveries from our search. This list of sources is provided in Table 4.1.

4.3 Observations and Methods

4.3.1 GMRT Data Reduction

We observed 6 of our targets (Abell 1914, SDSS-C4-DR3-3088, Abell 2593, CIZAJ1926.1+4833, Abell 2751, Abell 661) with the GMRT at 325 MHz and 610 MHz (project code 31_018 and 33_014). For the remaining 16 sources (Abell 2048, Abell 1033, Abell 133, Abell 85, 24P73, Ophiuchus, Abell 2256, Abell 1931, MaxBCG J217.95869+13.53470, Abell 725, Abell 4038, MKW8, Abell 565, Abell 2675, Abell 272, Abell 566), we used archival observations. Note that, Abell S753, Abell 2443 and Abell 13 lack legacy GMRT observations. See Table 4.2 for the observation details. We processed the GMRT data with the SPAM pipeline (Intema et al. 2017) that includes radio frequency interference (RFI) mitigation schemes, direction-dependent calibration, and ionospheric modelling (Intema et al. 2009). The final images of these sources are shown in Figure 4.3. The flux densities were set to the scale from Scaife & Heald (2012). A conservative 10% uncertainty was adopted for the flux density scale bootstrapping (Chandra et al. 2004) and was added quadratically to the uncertainties of all flux density measurements from the GMRT observations.

4.3.2 LOFAR Data Reduction

For 10 sources, we obtained LOFAR data at 144 MHz and they were observed in HBA_DUAL_INNER mode. 5 sources were observed as part of the LoTSS (Shimwell et al. 2017; Shimwell et al. 2019) and the other 5 targets were observed through pointed observations (project codes: LC0_037, LC6_015, LC9_027 and LC11_015). See Table 4.2 for the observation details. The standard direction-independent (DI) pipeline² (see de Gasperin et al. 2019 for the latest version) was used to correct for the DI effects, as described in detail in van Weeren et al. (2016a) and Williams et al. (2016). After the DI calibration was completed, the data were processed with the version 2.2 of the direction-dependent (DD) calibration and imaging pipeline in order to correct for DD effects. This is going to be described in detail in Tasse et al. (in prep) and is summarised briefly in Shimwell et al. (2019). This pipeline uses kMS (Tasse 2014, Smirnov & Tasse

²<https://github.com/lofar-astron/prefactor>

2015) for DD calibration and DDFacet³ (Tasse et al. 2018) for imaging with direction dependent calibration solutions applied.

A further post-processing step is conducted to subtract all the sources except for those in the vicinity of the targets and to perform additional phase and amplitude self-calibration loops for each target. This method has already been used in recent LOFAR studies (Hardcastle et al. 2019, Cassano et al. 2019, Botteon et al. 2019) and will be described in detail in van Weeren et al. (in prep.). Final images were processed by using WSCLEAN v2.8 (Offringa et al. 2014) with multi-scale multi-frequency deconvolution mode (Offringa & Smirnov 2017). The resulting images (see the legends) are shown in Figure 4.3.

Due to inaccurate beam models, the LOFAR flux scales are inaccurate and need to be corrected by comparison with other surveys (van Weeren et al. 2016b, Hardcastle et al. 2016). Here, we used catalogues from the TGSS Intema et al. (2017) to cross-match point sources near the target and compare the flux densities, similar to the approach used by Botteon et al. 2018b, Wilber et al. 2018, Mandal et al. 2019.

4.3.3 VLA Data Reduction

MKW8 has been observed with the VLA in the 1–2 GHz frequency band (project code: SH0396), with the B-, C- and D-configuration for a total time of 9 hrs (2, 5 and 2 hrs, respectively). The VLA data reduction follows the procedure as described in Di Gennaro et al. (2018). The calibration solutions were then applied to the target, and several self-calibration runs were performed to refine the amplitude and phase calibration. During these runs, automatic clean masks were employed with the PYthon Blob Detector and Source Finder (PYBDSF; Mohan & Rafferty 2015). Additional rounds of self-calibration were performed optimized for a bright source located outside of the primary beam, whose side-lobes were affecting the quality of the image. These self-calibration rounds were done by pre-subtracting all other sources in the field of view. The off-axis interfering source was then subtracted using these optimized self-calibration solutions from the uv-data. Final calibration uncertainties are of the order of 3% for the flux density scale.

4.3.4 X-ray Data Reduction

Three of the sources (Abell 2593, SDSS-C4-DR3-3088 and 24P73) were observed with *Chandra* ACIS-I in VFaint mode as part of the Guaranteed Time Ob-

³<https://github.com/mhardcastle/ddf-pipeline>

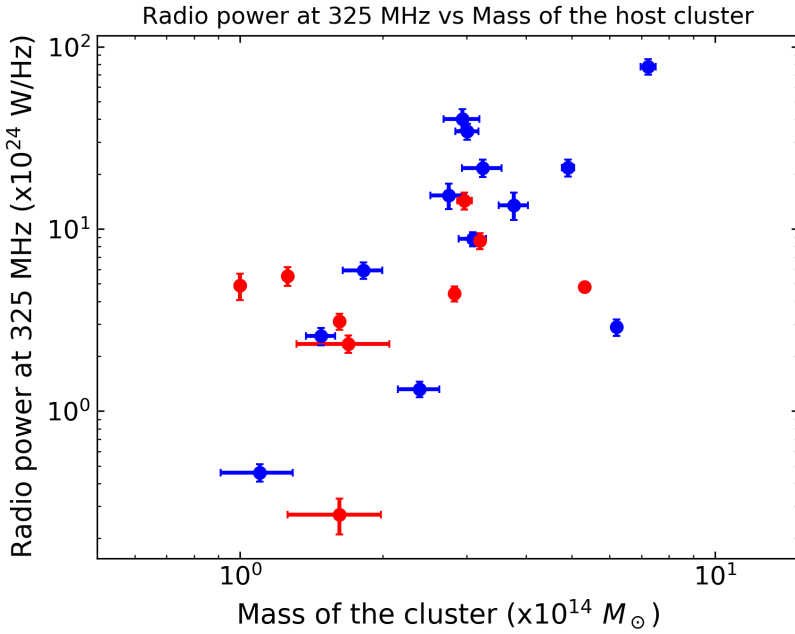


Figure 4.1: Radio power at 325 MHz for the sources in our sample as a function of the M_{500} of the host cluster. The values of M_{500} of the blue data points are from [Planck Collaboration et al. \(2016\)](#). The red data points correspond to the values of M_{500} that are taken either from [Piffaretti et al. \(2011\)](#) or derived using the scaling relations from [Arnaud et al. \(2005\)](#). See Table 4.3 for the details. The obtained Pearson and Spearman correlation coefficients from this plot are 0.48 ± 0.02 and 0.36 ± 0.08 , respectively.

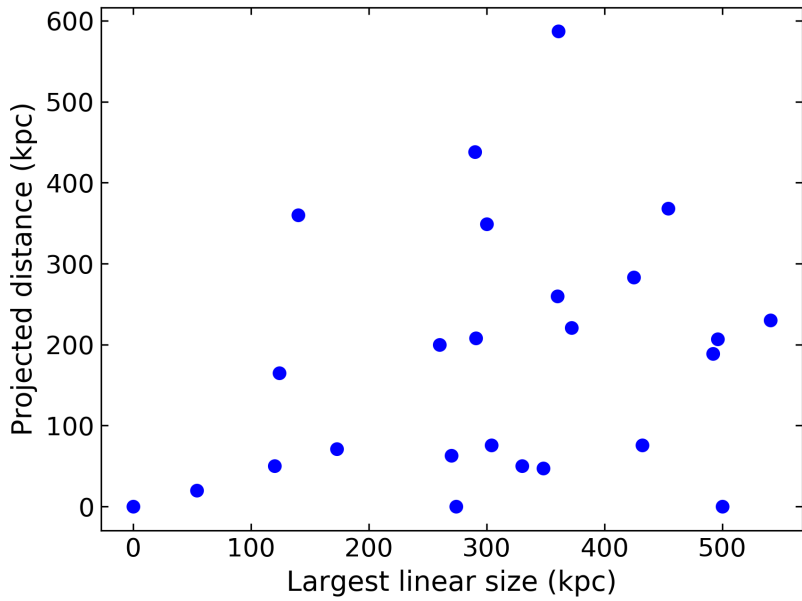


Figure 4.2: Projected distances of the radio phoenixes from the cluster centre as a function of their largest linear scales (LLS). The obtained Spearman and Pearson correlation coefficient are 0.26 ± 0.20 and 0.31 ± 0.13 respectively. See Section 4.4 for the details on how the cluster centre has been defined for this analysis.

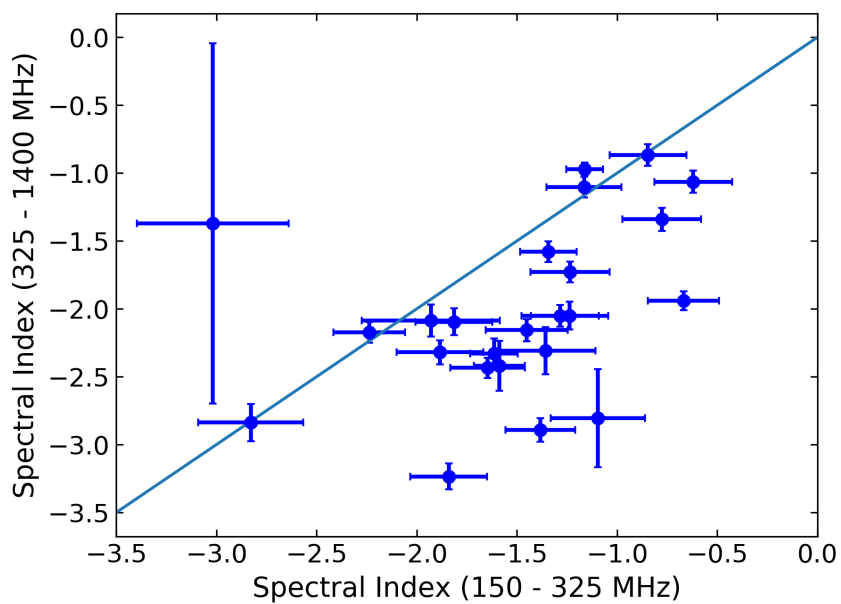


Figure 4.3: Color-color diagram for all the radio phoenixes presented in this paper. The measured flux densities (with associated error bars) and the spectral indices at different frequencies are provided in Appendix 4.5 and Table 4.4, respectively. The light blue line shows the 1:1 line.

servers (GTO) program (Obs IDs 20780, 20781 and 21710, respectively). For the rest of the sources from the sample of 25 sources, we searched in the *Chandra* and *XMM-Newton* archives for pointed observations. See Table 4.2 for the observation summary. Data were retrieved and processed with *Ciao* v4.12 (CalDB v4.9.0) and *SAS* v16.1.0 following standard reduction recipes, with the aim of obtaining exposure corrected cluster images in the 0.5 – 2.0 keV energy band. The X-ray images overlaid with contours from radio images are presented in Figure 4.3. These images were used to determine the position of the radio phoenixes in the clusters and qualitatively constrain the dynamical state of the host clusters.

4.3.5 Integrated spectral index

Due to the lack of homogeneous data available for the radio phoenixes, performing detailed spectral analysis of the sample is beyond the scope of this paper. In this paper we study the integrated spectral indices of the sources and investigate the spectral behaviour in between 150 MHz and 1.4 GHz. To sample the same spatial scales at 150 MHz and 325 MHz, we used the same inner uv -range of 200λ to image both LOFAR and GMRT data. For the sources that do not have any LOFAR 150 MHz data, we measured the total flux densities from the TGSS (Intema et al. 2017) images. Similarly, we used the NVSS (Condon et al. 1998) images to measure the total flux densities at 1.4 GHz. List of the measured flux densities at different frequencies and the source of these values are provided in Appendix 4.5.

4.4 Results

To date, 14 (candidate) radio phoenixes were known to exist in clusters. Our search yielded 11 new revived fossil plasma sources. Three out of 11 sources had been presented in detail in Mandal et al. (2019) and Mandal et al. (2020). This paper presents a sample of all radio phoenixes known to date to investigate the global physical properties of these sources and to understand the physical origin of this class. In Table 4.2 the observation details are provided. Table 4.3 shows a selection of derived / measured global properties of the host cluster. We have taken the mass of the host cluster from the Planck (Planck Collaboration et al. 2016) and MCXC (Piffaretti et al. 2011) catalogues (Note: the M_{500} values taken from the MCXC catalogues do not include any error bars). For Abell 2593, SDSS-C4-DR3-3088 and Abell 2048, we derived the mass by

using the X-ray luminosity and the scaling relations of [Arnaud et al. \(2005\)](#) (see [Mandal et al. 2020](#) for the details). Figure 4.3 shows the images of these radio phoenixes (which are marked with black ellipses) derived from the observations (as reported in Table 4.2). Note that, no radio images have been shown for Abell 13 and Abell S753, since they do not have LOFAR / GMRT data. Figure 4.3 and 4.4 shows the contour images of these sources overlaid on X-ray (*Chandra* or *XMM-Newton*) and optical (2nd Digitized Sky Survey Red) maps, respectively. The optical images are marked with black circles that show possible galaxies that could have originated the plasma associated with the diffuse radio emission (See Section 4.5 for more details). This association has been done by inspecting morphological connection with an optical counterpart and the respective redshift information.

First, we describe each of the 8 newly discovered sources and followed by briefer descriptions of sources that were previously known:

New Discoveries

- CIZAJ1926.1+4833 is a low-mass ($M_{500}=3.09^{+0.19}_{-0.22} \times 10^{14} M_{\odot}$) galaxy cluster located at $z = 0.098$ ([Planck Collaboration et al. 2016](#)). The 325 MHz GMRT image shows the presence of a bright radio source in the west of the cluster with a complex filamentary morphology. This radio source has an integrated spectral index of $\alpha_{325-1400} = -2.32 \pm 0.11$ and $\alpha_{150-325} = -1.61 \pm 0.12$, indicating that the spectra is curved towards higher frequency. To the SE (with respect to the source) we also identify a very long head tail galaxy (about 770 kpc). The tail of this galaxy is very faint at the 610 MHz (figure in Appendix 4.A). The X-ray emission (from *XMM-Newton*) is not peaked at the centre, suggesting that the dynamical state could be somewhat disturbed.
- MKW8 is a poor galaxy cluster ($M_{500}=1.10^{+0.18}_{-0.20} \times 10^{14} M_{\odot}$) located at $z = 0.027$ ([Planck Collaboration et al. 2016](#)). Previous radio observations ([Bharadwaj et al. 2014](#)) reported the presence of a central compact bright radio source NGC 5718 (one of the BCG's; marked with a black circle in Figure 4.4). Our LOFAR 150 MHz image shows previously undetected diffuse radio emission (located ~ 50 kpc towards NW side of NGC 5718) which has an extremely steep spectrum ($\alpha_{150-1400} = -2.75 \pm 0.06$) and filamentary morphology. A GMRT 610 MHz image is shown in the Appendix A where the diffuse emission is barely visible. [Tümer et al. \(2019\)](#)

did not find any presence of a cool core and classified MKW8 as a disturbed system. Using wide-band VLA observations, we investigated the polarisation properties of MKW8 (see Appendix 4.A for the VLA Stokes I image of MKW8). The total linear polarised intensity image, averaged in the 1–2 GHz band, was obtained with the `pyrmsynth tool`⁴ (see Di Genaro et al. submitted for the details). No evidence of polarised emission is detected in this source. We estimated an upper limit for the polarisation degree of 0.8%.

- Abell 565 is a low-mass cluster ($M_{500}=1.62 \times 10^{14} M_{\odot}$) located at a redshift of $z = 0.105$ (Piffaretti et al. 2011). The GMRT 325 MHz map shows that the radio emission has a complex and filamentary morphology. The radio phoenix candidate has a spectral index of $\alpha_{150-1400} = -1.79 \pm 0.05$. The BCG of the cluster (WISEA J070819.13+715224.7) is morphologically connected with the diffuse radio emission (marked with a black circle in Figure 4.4). There is no dedicated X-ray observation available for this cluster and, as a result, we classify the dynamical state of this cluster as uncertain.
- Abell 2675 ($M_{500}=2.39_{-0.23}^{+0.25} \times 10^{14} M_{\odot}$; Planck Collaboration et al. 2016) is located at a redshift of $z = 0.071$. In the *XMM-Newton* X-ray image of this cluster, we do not detect any peaked X-ray emission at the centre and classify it as an un-relaxed system. The BCG of the system (WISEA J235542.59+112035.5) is the most likely candidate associated with the diffuse radio emission. The measured integrated spectral indices of the source are $\alpha_{325-1400} = -1.72 \pm 0.08$ and $\alpha_{150-325} = -1.23 \pm 0.20$.
- Abell 272 ($z = 0.088$) is a low-mass galaxy cluster ($M_{500}=2.83 \times 10^{14} M_{\odot}$; Piffaretti et al. 2011). The two bright X-ray peaks are associated with two cluster members: ZwCl 0152.0+3337 06 & ZwCl 0152.0+3337 08 which are marked as X1 and X2, respectively, in Figure 4.4. The LOFAR 150 MHz radio image shows an elongated morphology in the north-south direction. The elongated feature is also visible in the GMRT 325 MHz image (shown in Appendix 4.A). However, some of the diffuse emission that is visible at 150 MHz, is not well recovered at 325 MHz, suggesting that its spectrum is steep. The measured integrated spectral indices are $\alpha_{325-1400}$

⁴<https://github.com/mrbell/pyrmsynth>

$= -2.43 \pm 0.07$ and $\alpha_{150-325} = -1.64 \pm 0.18$. We locate three galaxies that are morphologically connected with the radio emission and are cluster members: A (ZwCl0152.0+3337 03), B (ZwCl0152.0+3337 04) and C (ZwCl0152.0+3337 05). The X-ray emission (see Figure 4.3) does not appear to be peaked, hence we classify it as an un-relaxed system.

- Abell 566 ($z = 0.097$) was known (Harris et al. 1982) to host a very steep-spectrum object: 4C63.10 ($\alpha_{38-408} \sim -1.7$). In the GMRT 325 MHz image presented in this paper, we find two BCGs of this cluster (marked as ‘A’: ZwCl 0658.3+6320 e and ‘B’: ZwCl 0658.3+6320 a in the optical image). The location of the brightest radio emission coincides with the position of the host galaxy ‘A’. The measured integrated spectral indices of this source are $\alpha_{325-1400} = -2.32 \pm 0.09$ and $\alpha_{150-325} = -1.88 \pm 0.21$, indicating that the spectra is curved towards higher frequency. We do not have pointed *Chandra* or *XMM-Newton* observations of this source. In the Appendix 4.A, we showed a Suzaku X-ray image of this cluster. Even though the cluster has regular morphology, it is not peaked at the centre suggesting the dynamical state could be un-relaxed. This needs to be confirmed with dedicated *Chandra* or *XMM-Newton* observations in future.
- Abell 2751 ($z = 0.107$) is a very low-mass galaxy cluster ($M_{500} = 1.26 \times 10^{14} M_{\odot}$; Piffaretti et al. 2011) that has peculiar radio emission. Towards the west, we identify an elongated region extending towards the south. The brightest part of the radio emission has an optical counterpart with a galaxy (marked as ‘A’: PKS 0013-316 in the optical image). The measured integrated spectral indices of the diffuse, filamentary region towards the east side of the cluster are $\alpha_{325-1400} = -1.34 \pm 0.09$ and $\alpha_{150-325} = -0.77 \pm 0.20$. At this location, we identify an optical galaxy WISEA J001657.00-312134.9 (marked as ‘B’ in the optical image) that could be associated with the diffuse radio emission. Note that the source appears to have regions with a very steep spectral indices of ≤ -2 (de Gasperin et al. 2018).
- Abell 661 is located at a redshift of $z = 0.12$. The radio emission has three distinctive features and only part of the diffuse emission at the north is identified to have steep spectrum. From the north to the

south, we have identified three optical galaxies which are marked as ‘A’ (WISEA082708.33+531108.0), ‘B’ (WISEJ082720.91+530748.2) and ‘C’ (WISEJ082729.73+530733.5) in the optical image. The eastern part of the emission in the north has a very steep spectra (see Appendix for the GMRT 610 MHz map) and filamentary morphology. X-ray observations are needed in order to investigate the dynamical state of this cluster.

Previously known sources

- Abell 1914 is a well studied massive ($M_{500}=7.24_{-0.26}^{+0.26} \times 10^{14} M_{\odot}$; [Planck Collaboration et al. 2016](#)) galaxy cluster located at a redshift of $z = 0.17$. Recent LOFAR and GMRT observations ([Mandal et al. 2019](#)) showed the ultra-steep spectrum source (4C38.39), previously thought to be part of a radio halo ([Bacchi et al. 2003](#), [Govoni et al. 2004](#)), is a distinct source with properties that are consistent with radio phoenixes. *Chandra* observations ([Botteon et al. 2018a](#)) showed that Abell 1914 has a very disturbed morphology with possible shocks present. However, the shock is not located at the radio phoenix.
- In [Mandal et al. \(2020\)](#), we studied SDSS-C4-DR3-3088 ($z = 0.046$; [Simard et al. 2009](#)) and Abell 2593 ($z = 0.041$; [Ulmer et al. 1981](#)) in detail with radio (LOFAR and GMRT) and X-ray (*Chandra*) observations and classified them as radio phoenixes. SDSS-C4-DR3-3088 contains what looks to be a wide-angle radio tail. Abell 2593 has a morphology more similar to a narrow-angle radio tail. Both of them show filamentary structure with patchy spectral index along the source. The dynamical states of these clusters are not relaxed.
- [van Weeren et al. \(2009\)](#) followed up Abell 2048 ($z = 0.098$; [Struble & Rood 1999](#)) with GMRT and VLA observations and classified it as a relic radio source. In [Mandal et al. \(2020\)](#) we studied this cluster with additional LOFAR data and recovered more extended diffuse emission compared to previous studies. The dynamical state of this cluster was classified as un-relaxed with *XMM-Newton* observations.
- Abell 1033 ($z = 0.126$) is a moderately massive galaxy cluster that underwent a recent merger and [de Gasperin et al. \(2015\)](#) presented the detection

of a radio phoenix close to the moment of its formation. Later, with the help of GMRT and LOFAR observations, [de Gasperin et al. \(2017\)](#) detected another ultra-steep spectrum source that is related with the cluster merger and classified as a gently re-energized tail (GR_{ET}).

- The radio phoenix in Abell 2443 ($z = 0.108$) was first shown in [Cohen & Clarke \(2011\)](#). Later, with deep *Chandra* observations, [Clarke et al. \(2013\)](#) demonstrated that the cluster is highly disturbed. A tentative shock at the location of the radio phoenix was also reported.
- [Slee et al. \(2001\)](#) presented results from 1.4 GHz observations of four sources in the clusters: Abell 133 ($z = 0.057$), Abell 85 ($z = 0.055$), Abell 13 ($z = 0.094$) and Abell 4038 ($z = 0.028$). Even though Abell 133 has been identified as a cool-core cluster ([Cavagnolo et al. 2009](#)), *Chandra* observations showed presence of dynamical disturbance ([Randall et al. 2010](#)). The X-ray emission in Abell 85 is peaked at the centre, however, *XMM-Newton* observations have shown the presence of dynamical activity revealing that it is not fully relaxed ([Durret et al. 2005](#)). Abell 13 has been classified as a system that has undergone a recent merger ([Juett et al. 2008](#)). [Kale et al. \(2018\)](#) showed an absence of a cool core in Abell 4038 and classified it as an un-relaxed system. In this work, we have shown GMRT 325 MHz images for Abell 133 and Abell 85. These 325 MHz images reveal much more extended emission compared to the ones presented by [Slee et al. \(2001\)](#) at 1.4 GHz. Note that we do not show any image for Abell 13 in this paper. The 325 MHz flux measurements are taken from [Joshi et al. \(1986\)](#).
- The radio source 24P73 was found to have an unusually steep spectrum ([Green & Joncas 1994](#)) and [van Weeren et al. \(2011\)](#) classified it as a radio phoenix. The galaxy cluster associated with this source is currently not confirmed due to high extinction from the Galactic plane. However, using Hubble-R relation, [van Weeren et al. \(2011\)](#) estimated a redshift of this source to be $z = 0.15 \pm 0.1$. Recently this source has been observed with *Chandra* and the resulting image is shown in Figure 4.3. We do not detect any peaked X-ray emission at the centre of the cluster and classify as un-relaxed system.

- [Kempner & Sarazin \(2001\)](#) detected diffuse radio emission in Abell 725 ($z = 0.09$) from the WENSS. In this paper we have shown the 325 MHz GMRT image of the source. The brightest radio source is associated with the elliptical galaxy (marked in the optical image). The diffuse radio emission located towards the north-eastern side of this elliptical galaxy (marked with a circle in the radio image), has an ultra-steep spectrum. The X-ray gas is thought to be slightly elongated along the axis connecting the ultra-steep spectrum source and the cluster centre ([Kempner & Sarazin 2001](#)).
- The Ophiuchus cluster is located at a redshift of $z = 0.028$ and is the second brightest galaxy cluster in the X-ray sky. With deep *Chandra* observations, [Werner et al. \(2016\)](#) showed that the core of the cluster is dynamically disturbed with multiple sloshing induced cold fronts. Their deep 1.4 GHz map reveals the presence of a very filamentary source towards the NE of the cluster centre, that was classified as a radio phoenix. Similar features were also reported in [Murgia et al. \(2010\)](#).
- Abell 2256 ($z = 0.058$) is a well-studied massive galaxy cluster that is presently undergoing a merger with a smaller sub-cluster. Even though the main focus of studies of this cluster in the past has been the radio relic, halo and the long head-tail galaxy, this system is known to host ultra-steep spectrum sources. ‘Source F’ is one of the objects that was discovered by [Bridle et al. \(1979\)](#) and classified as a radio phoenix by [van Weeren et al. \(2012a\)](#). This source is located towards the east of the main relic. In this paper, we have shown the 325 MHz image of this source.
- Abell 1931 ($z = 0.17$) is a low-mass ($M_{500}=1.62_{-0.72}^{+2.04} \times 10^{14} M_{\odot}$) galaxy cluster. The *Chandra* image of this cluster is not peaked at the centre (see Figure 4.3) and hence is classified as un-relaxed. With the use of LOFAR 150 MHz data, [Brüggen et al. \(2018\)](#) showed the presence of diffuse ultra-steep emission in this cluster that has not been detected in 325 MHz and 610 MHz. A bright, red elliptical galaxy (SDSS J143212.84+441620.4) was claimed to be the BCG and a possible host for the diffuse emission.
- MaxBCG J217.95869+13.53470 ($z = 0.16$) is a low-mass ($M_{500}=1.00 \times 10^{14} M_{\odot}$) galaxy cluster that is undergoing a merger event. With GMRT

325 MHz & 610 MHz observations [Ogrea et al. \(2011\)](#) showed the presence of a radio phoenix towards the SW of the cluster that is not associated with X-ray or optical emission. However, a bridge of faint radio emission is connected with the central radio source (AGN). [Shulevski et al. \(2015\)](#) presented a low-frequency spectral index map between 150 and 325 MHz of this source, that does not show signs of patchiness in the spectral indices. However, the source is only a few beam-widths across and beam smearing can play a roll.

- Abell S753 ($z = 0.014$) is known to have an ultra-steep spectrum radio source: PKS B1400–33 ([Sarazin 2013](#)). [Subrahmanyan et al. \(2003\)](#) presented the VLA 330 MHz and ATCA 2.4 GHz observations and identified the bright X-ray emission in this cluster to be associated with NGC 5419. The radio source has an integrated spectral index of < -1.4 between 85 MHz and 330 MHz and tends to get steeper (~ -2) at higher (2.4 GHz) frequency, suggesting a possible curved spectrum. Note that we do not show any image for Abell S753 and refer to [Subrahmanyan et al. \(2003\)](#).

4.5 Common properties

In this section, based on the results presented in Section 4.4, we list physical properties of the radio phoenixes.

Connection with an AGN?

A key question that needs to be answered is what is the source of these fossil electrons in the ICM? It is clear that galaxy clusters host a number of radio galaxies that have an active galactic nuclei (AGN). In the results section, we showed the presence of nearby optical galaxies / AGNs that belong to the host cluster and have a tentative morphological connection with the diffuse radio emission. The possible optical counterparts of these AGNs are marked in Figure 4.4. Note that, a morphological connection with an optical counterpart is not obvious for the sources: Abell 2443, 24P73, Ophiuchus, MKW8 and MaxBCG J217.95869+13.53470. Indeed, the plasma from an AGN can move in the ICM with respect to its source of origin, making the identification of optical hosts harder ([Duchesne & Johnston-Hollitt 2019](#), [Randriamanakoto et al.](#)

2020). At the location of the (possible) optical counterparts, the spectral index value (Abell 1914, SDSS-C4-DR3-3088, Abell 2593, Abell 2048, Abell 1033, Abell 2443, Abell 133, Abell 2256, Abell 4038; see Table 4.1 for references) is flatter (~ -0.8) which is in agreement with the expectation from the lobes of an active AGN.

Radio power of the source and mass of the host cluster

Studying the correlation of thermal and non-thermal components in clusters can be useful to understand the dynamics in the ICM. Since deep radio data at 325 MHz is available for a large fraction of the whole sample of radio phoenixes, we calculated the k -corrected 325 MHz radio power $P_{325\text{MHz}} = 4\pi S_{325\text{MHz}} D_L^2 (1+z)^{-(\alpha+1)}$ (the values of the measured flux densities and radio powers with associated errors are reported in the Appendix 4.5). The spectral indices of these sources vary over the frequency range from 150 MHz to 1.4 GHz (See Table 4.4). Therefore, we used a conservative value of the spectral indices from -2 to -1.5 to calculate the k -corrected radio power. It is important to note that, using this range of spectral indices, does not change the value of the derived radio power significantly, given the fact that these sources reside in nearby Universe. Using the mass reported in Table 4.3, we have investigated if there is a trend between the derived radio power at 325 MHz as a function of the mass (M_{500}) of the host cluster (see Figure 4.1). The values of the Pearson (0.48 ± 0.02) and Spearman (0.36 ± 0.08) and correlation coefficients do not suggest a strong correlation between these two measured quantities.

Position and Size of the sources

Previous studies of radio relics found that they are usually located in the outskirts of clusters and that there is a correlation between the largest linear size (LLS) and the distance from the cluster centre (de Gasperin et al. 2014). We therefore compare the LLS of the radio phoenixes with the projected distance from the cluster centre. Since the morphologies of these radio phoenixes are very filamentary and irregular compared to radio halos and radio relics, robustly estimating the ‘position of the source’ from a reference point is not trivial. Therefore, by analogy with centre of mass, we define a parameter ‘centre of intensity’ which can be described as a unique point where the weighted relative position of the distributed flux densities sums to zero. The regions of the emission that go into these calculations are also marked in the radio images. We take the contribution of the whole emission from the ‘phoenix’ source into account. If

the flux density at a location (x,y) is $I(x,y)$, the co-ordinates of the centre of intensity (X and Y) are:

$$X = \frac{\sum I(x,y) \times x}{\sum I(x,y)} \quad (4.1)$$

$$Y = \frac{\sum I(x,y) \times y}{\sum I(x,y)} \quad (4.2)$$

Having found this position, the distance from the cluster centre is then calculated as the distance from the location of the pixel with the brightest emission in X-ray, from (X,Y) . The plot of projected distance vs LLS is shown in Figure 4.2. We do not find any strong correlation between these two measured parameters. The measured Spearman and Pearson correlation coefficients are 0.26 ± 0.20 and 0.31 ± 0.13 , respectively. Note that we have used the RASS data for the sources that do not have any *Chandra* or *XMM-Newton* observations. We have also reported the values of R_{500} in Table 4.3. We note that the radio phoenixes are all located well within R_{500} of their host clusters.

Dynamical state of the host cluster

In Figure 4.3, we show the X-ray images overplotted with the contours from the radio emission (in white). Images of only 18 sources are shown that have dedicated X-ray observations (See Table 4.2 for the summary of the observation details and Section 4.3 for the method of data reduction). Visual inspection of X-ray images is one of the qualitative ways that can be used to identify dynamical state of a cluster (Lovisari et al. 2017). Based on our visual inspection of the X-ray emission and on the literature studies, we have summarised the dynamical state of these systems of galaxy clusters in Table 4.3. For a more quantitative analysis, it is important to study morphological parameters (such as centroid shift, concentration parameters, power ratios etc.) of a cluster. However, homogeneous deep X-ray data would be highly advantageous for this purpose.

We see that all the 19 sources out of 25 sources that have pointed observation reside in somewhat dynamically un-relaxed clusters. Systematic deep X-ray observations will follow in future to characterise the dynamical state of the clusters more accurately and map the temperature in different regions.

Spectral properties

While sources in our sample have ultra-steep spectrum by selection, also all the previously known radio phoenixes show an overall ultra-steep radio spectrum. Previous literature studies found that the spectral index measurements from different observations tend to show a hint of a curved spectrum towards high (\sim GHz) frequencies (Slee et al. 2001, Cohen & Clarke 2011, de Gasperin et al. 2017, Kale et al. 2018, Mandal et al. 2019, Mandal et al. 2020). For the newly discovered sources, a hint of spectral steepening is also noticed while comparing the spectral index measurements from 150 MHz (TGSS or LOFAR) to 325 MHz and 325 MHz to 1.4 GHz (NVSS) measurements. The measured total flux densities are listed in Appendix 4.5. See Table 4.4 for the values of spectral indices as measured from these flux density measurements. In order to investigate the overall spectral shape, we used so called three frequency ‘color-color’ plots which is shown in Figure 4.3. Here, we have plotted the high-frequency spectral indices ($\alpha_{325-1400}$) vs the low-frequency spectral indices ($\alpha_{150-325}$). The light blue line shows 1:1 line. The fact that most of the sources lie below the identity line, shows that these sources have a curved spectrum towards high frequencies. However, it is important to note here that deeper high resolution, i.e. VLA 1.4 GHz observations are important to confirm this claim.

4.6 Discussion

In the last decades, the taxonomy of (diffuse) radio sources has become clearer. However, in many cases for example, the distinction between ‘radio relics’ and ‘radio phoenixes’ was not evident. For instance, some of the present day radio relics (Abell 2256, Abell 3667 etc.) were previously thought to be in the category of radio phoenixes. Statistical follow-up observations of radio relics have made the contrast with radio phoenixes clearer. However, radio phoenixes are still a poorly studied class of the population of diffuse cluster radio sources. Here we discuss insights obtained from the observations and results presented in the previous sections.

Source of relativistic particles: AGN origin

From the optical maps presented in Figure 4.4, we observe that (most of) these sources are morphologically connected with an AGN (radio galaxy) which implies that lobes and tails of radio galaxies in clusters are likely candidates for the

source of relativistic particles that power radio phoenixes. The typical length scales of these phoenixes are $\leq 500\text{--}600$ kpc (see Table 4.4 for the LLS of the phoenixes). A definite identification of the host galaxy for these sources is not trivial. However, we find that in general, nearby elliptical galaxies are more likely candidates to be associated with these phoenixes. Although, the BCGs could also be a possible candidate for the source of seed particles (for ex: Abell 133, Abell 725, MKW8 etc.).

Location of the phoenixes in the cluster

An interesting result is that all the radio phoenixes are located well within the R_{500} (at least in projection) of the cluster (See Table 4.3 and 4.4 for the R_{500} and the distance from the cluster centre, respectively).

In the inner regions of clusters, the pressure of the ICM is higher compared to the outskirts. These high pressure environments do not allow the free expansion of the fossil radio plasma and the plasma remains more confined (Parma et al. 2007, Murgia et al. 2011). Thus, low-frequency radio emission from these fading plasma can last longer if their expansion is reduced by the high pressure environment. In addition, if the expansion of the lobes is prevented, the synchrotron losses are expected to be much higher due to the higher internal magnetic fields (Bonafede et al. 2011) of pressure confined radio plasma. As a result, the radio source could exhibit ultra-steep spectrum. On the contrary, if radio plasma lives in the cluster outskirts, the ambient environment is not dense enough to prevent the expansion of the lobes into the ICM. Due to the expansion, the strength of the internal magnetic field also decreases, and so as the radiative losses. Therefore, the radio emission can become too faint to be detected, even at the lower-frequencies. For these reasons, steep-spectrum radio phoenixes are more likely to be found in dense environments. This is also one of the key differences when compared to radio relics which tend to reside in cluster outskirts (Feretti et al. 2012, van Weeren et al. 2019).

Spectral behaviour and acceleration mechanism

In Table 4.4, we reported the values of the integrated spectral indices of the radio phoenixes. Figure 4.3 shows the variation of high-frequency spectral indices ($\alpha_{325\text{--}1400}$) with respect to the low-frequency spectral indices ($\alpha_{150\text{--}325}$). Most of the sources lie below the 1:1 line in this three frequency color-color diagram indicating that the spectral indices are flatter at the lower (between 150 – 325 MHz) frequencies and steeper at higher (between 325 – 1400 MHz) frequencies;

i.e. in general the radio phoenixes show spectral steepening at higher frequencies similar to the lobes of remnant radio galaxies that also have a curved spectra (Murgia et al. 2011, Brienza et al. 2016) due to IC and radiative losses.

It has been shown that in the absence of dynamical processes, low-energy relativistic electrons from lobes of radio galaxies can be poorly mixed with the thermal ICM (Sarazin 1999; Petrosian 2001; Pinzke et al. 2013). Therefore, temperature inside the radio plasma (that is mixed with the thermal plasma) increases and also the sound speed is high. Under these conditions, a weak shock in the ICM will not transfer as a shock in the lobe. Instead of shock re-acceleration, it can compress these old lobes of radio galaxies adiabatically (Ensslin et al. 1998, Enßlin & Brüggen 2002). Compression only shifts the spectral shape of the spectrum towards higher frequencies and does not change the underlying shape of the electron population.

It is important to note here, that all the previously known radio phoenixes tend to show a patchy distribution of spectral indices (see the respective references on Table 4.3 for the spectral index maps). They do not have a clear gradient in their spectral indices across the source⁵. This might be a key difference with merely aged tails from (remnant) radio galaxies that show instead a spectral gradient across the lobes (Murgia et al. 2011, Shulevski et al. 2017). On the other hand, as a contrast, radio relics also show spectral gradient and their spectrum follow a power-law distribution (van Weeren et al. 2019, Rajpurohit et al. 2020).

Therefore, for the phoenixes, this suggests a possible mix of cosmic-ray particles that have different ages and losses. This in-homogeneous mixing of the ICM and the relativistic particles from an AGN also implies an averaging of the effective adiabatic index ($\frac{4}{3} < \gamma_{ad} < \frac{5}{3}$) that could lead to different adiabatic compression ratios and re-acceleration efficiencies across the source. Hence, even if we find that radio phoenixes tend to follow a curved spectra, these sources should not be thought of a reservoir of uniform cosmic-ray population.

Dynamical state of the host cluster

We find that 19 out of 25 sources in our sample (the rest of the sources do not have pointed X-ray observations and hence, no information is available) are residing in clusters that are dynamically un-relaxed (See Table 4.3 for a

⁵Although, some of the newly discovered sources lack multi-frequency radio data to create resolved spectral index maps that are essential to investigate spatial variation of spectral indices.

summary and Section 4.4 for the method of qualitative determination of the dynamical states).

Dynamically un-relaxed clusters have (weak) shocks and ICM bulk motions which can affect ghost plasma from radio galaxies (Jones et al. 2017a). In line with our observations, recent simulations (Nolting et al. 2019 and O’Neill et al. 2019) have shown that old radio lobes in presence of (weak) shocks and/or relative motion with respect to the ICM can show filamentary morphologies and curved spectra. However, it is important to note that, to date, there has not been a clear detection of a shock at the location of a radio phoenix. The lack of a detection of a shock could potentially be related to our finding that these phoenixes are mostly located within the R_{500} of a cluster. The Mach number of a merger shock and its surface area increase with the distance from the cluster centre (Vazza et al. 2012). Which essentially means, the central regions of the ICM are crossed by weak shocks and they are much harder to be detected (Botteon et al. 2018a).

Scaling relations

Studying the correlation between thermal and non-thermal components helps to understand the dynamics in the ICM. For radio halos and relics it has been found that the measured radio power and the mass (M_{500}) of the host cluster are correlated (radio halos: Cassano et al. 2010, Cassano et al. 2013; radio relics: de Gasperin et al. 2014, Brüggén & Vazza 2020). For radio phoenixes, we do not notice any strong correlation between these two quantities (reported in Figure 4.1). Also, we see that only four (Abell 1914, Ophiuchus, Abell 2256 and Abell 85) out of 25 sources, are located in (moderately) massive clusters; the rest are mostly residing in lower-mass systems. The fact that these systems seem to be located mostly in lower-mass systems could be because low-mass clusters are more abundant than massive clusters. Indeed, clusters with mass $> 4 \times 10^{14} M_{\odot}$ are rare in the local Universe (Planck Collaboration et al. 2016) and our sample is mainly driven by the TGSS, which is sensitive only to the luminous sources that are nearby.

In addition, we also do not find any correlation between the distance from the cluster centre with the largest linear scales of the radio phoenixes (see Figure 4.2). This is also in contrast with the scaling relations found by Bonafede et al. (2012) and de Gasperin et al. (2014) for radio relics. The fact that there is a lack of correlation between these measured quantities suggests that the formation of these sources do not directly depend on the energy released due to the merger. Rather, their formation may be more closely related to the state of AGN activity

for respective cases.

It is important to note here that recently it has also been found that smaller radio relics can occur at the periphery of clusters (Nuza et al. 2017) and analysing the ‘shape’ of radio sources as a function of the distance from the cluster centre could be a better proxy in order to distinguish radio relics and radio phoenixes. This will also enable us to understand the dynamics of the cluster and its relation with the non-thermal emission. Upcoming sensitive radio (such as LoTSS; Shimwell et al. 2019) and X-ray (eRosita) surveys will be crucial to address this question in an unbiased way.

Future study: polarization properties of radio phoenixes

In future, it will be important to observe these radio phoenixes at \sim GHz frequencies to determine the sources’ polarization fraction and the polarization angle. Simulations indicate that if these sources are indeed shock compressed, there should be a correlation between the total linear polarization and the viewing angle because of the magnetic field ordering (Enßlin & Brüggen 2002). In our sample, we could investigate the polarisation properties only for MKW8, being able to put an upper limit for the polarisation degree (i.e. 0.8%). It could be the case that the source is not intrinsically polarised. However, since the source is located near the cluster centre (\sim 50 kpc), it is likely that the source can suffer extreme depolarisation due to the ICM (Rotation Measure: $RM \propto \int n_e \times B_{\parallel} dl$, where n_e and $B_{\parallel} dl$ the electron density and the perpendicular component of the magnetic field integrated along the distance to the source L). We also do not detect polarized signal from the BCG of this cluster. Future wide S-band observations with the VLA would be crucial to determine if strong depolarization can occur from the ICM.

Drawing general conclusions on the polarisation properties for the whole population is beyond the scope of this paper. But we also notice that these phoenixes are located mostly towards the centre of the cluster (see the R_{500} values in Table 4.3). This suggests that the sources could be highly de-polarized. Also, if these sources are indeed associated with weak shocks, the expected alignment and amplification of the magnetic field are also less. Finally, given the fact that these phoenixes have a very steep spectra, they could be very faint at GHz frequencies. Therefore, statistical follow-up observations to study the polarisation may not be trivial.

4.7 Summary and conclusion

In this paper, we have presented an exploratory study in which we look for ultra-steep spectrum sources using the 150 MHz TGSS and the 1.4 GHz NVSS. Our search yielded 11 new discoveries that were followed up with radio and/or X-ray observations. Based on the results from these observations, we classify them in the category of radio phoenixes. In addition, to extend our sample of radio phoenixes and to be as complete as possible we inspected all the sources that are classified as ‘revived fossil plasma sources’ (referred as ‘F’ in the latest review by [van Weeren et al. 2019](#)). Sources that are resolved, have a filamentary morphology, have a steep spectrum ($\alpha \leq -1$) with a hint of a curvature towards high-frequency, were considered to be candidate phoenixes. We present the results from all the known or newly discovered radio phoenixes along with their common physical properties in order to establish the nature of this relatively unexplored class of objects. Below we summarize our findings:

- These radio phoenixes appear to have an AGN origin and are located well within the R_{500} of the cluster. This is one of the key differences when compared to radio relics that reside towards the outskirts of the cluster. The high-pressure environments inside the cluster region do not allow the free expansion of the fossil radio plasma (from an AGN), making it more confined. Also, synchrotron losses are greater inside the cluster, which could explain the unusually steep spectra of these sources.
- These sources show a spectral steepening towards high frequencies, suggesting the integrated spectra is curved. Also, they have spatially non-uniform spectral indices. So even if the phoenixes tend to follow a curved spectra, these sources should not be thought of a reservoir of uniform cosmic-ray population. Resolved spectral index maps are also crucial tools to distinguish between different class of diffuse radio sources and to probe the energy distribution of relativistic particles within a (radio) source.
- From the X-ray observations, we notice that 19 of the sources (6 out of 25 sources do not have pointed X-ray observations) tend to live in clusters that are dynamically un-relaxed, therefore supporting the scenario that these are associated with ICM motion and/or shocks.
- We find that 19 out of 23 sources (2 of the clusters do not have any measurements on their masses) are located in low-mass ($< 4 \times 10^{14} M_{\odot}$) clusters of galaxies. Also, for these sources, we compared: a) the 325 MHz

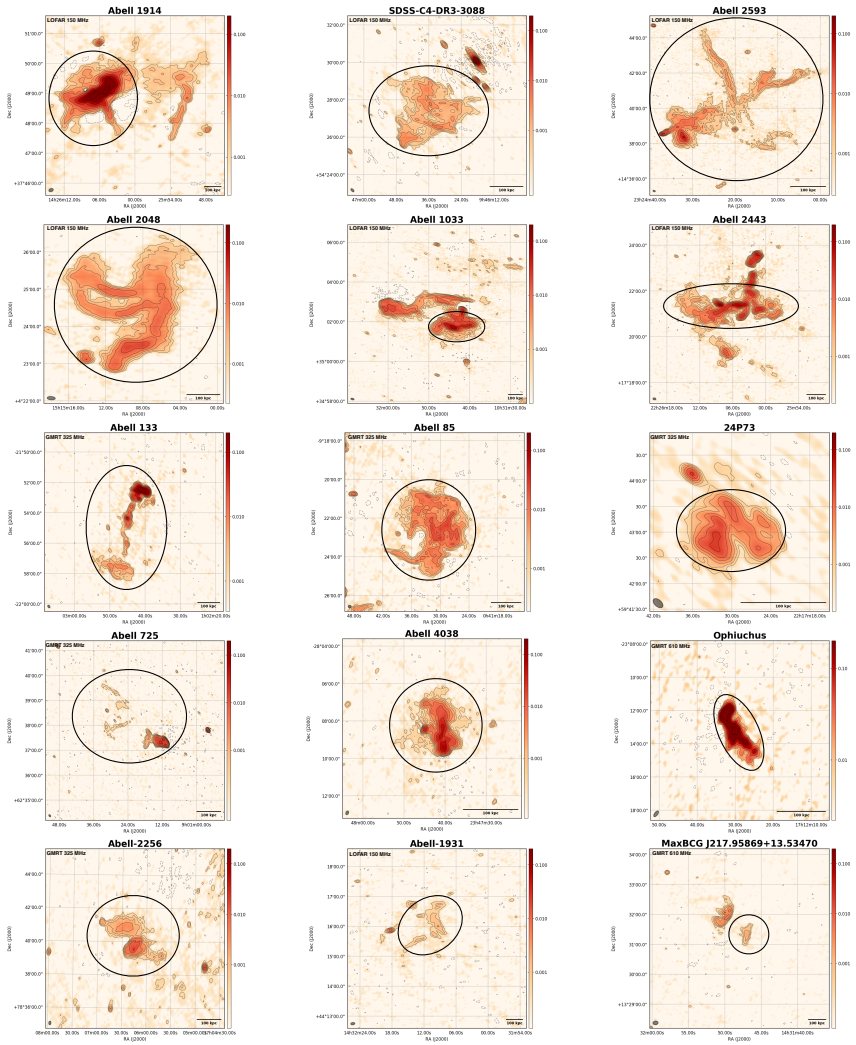
measured radio power as a function of the cluster mass, and b) the largest linear scale of the sources as a function of projected distance from the cluster centre. We do not notice any strong correlations between these measured quantities.

Our method to look for these ultra-steep spectrum sources in galaxy clusters was driven by the TGSS at 150 MHz and only the brightest sources were followed up which is necessarily the tip of the iceberg of this population. Future much deeper and sensitive low-radio-frequency surveys such as LoTSS at 144 MHz ([Shimwell et al. 2019](#)) & LoLSS at 53 MHz (de Gasperin et al. in prep) will be excellent tools to further investigate the nature of these fossil electron populations. Since these forthcoming surveys are an order of magnitude deeper in terms of both resolution and depth, they will most likely also be able to pick sources that are at higher redshift. Thus, it will be possible to compile a more unbiased and complete sample of radio phoenixes and investigate their occurrence rate in clusters.

Acknowledgments

This paper is based (in part) on data obtained with the International LOFAR Telescope (ILT) under project code LC0_037. LOFAR ([van Haarlem et al. 2013](#)) is the Low Frequency Array designed and constructed by ASTRON. It has observing, data processing, and data storage facilities in several countries, that are owned by various parties (each with their own funding sources), and that are collectively operated by the ILT foundation under a joint scientific policy. The ILT resources have benefitted from the following recent major funding sources: CNRS-INSU, Observatoire de Paris and Université d'Orléans, France; BMBF, MIWF-NRW, MPG, Germany; Science Foundation Ireland (SFI), Department of Business, Enterprise and Innovation (DBEI), Ireland; NWO, The Netherlands; The Science and Technology Facilities Council, UK ; Istituto Nazionale di Astrofisica (INAF), Italy. We thank the staff of the GMRT that made these observations possible. GMRT is run by the National Centre for Radio Astrophysics of the Tata Institute of Fundamental Research. This paper is based on the data obtained with the International LOFAR Telescope (ILT). The Leiden LOFAR team acknowledge support from the ERC Advanced Investigator programme NewClusters 321271 and the VIDI research programme with project number 639.042.729, which is financed by the Netherlands Organisation for Scientific Research (NWO). AD acknowledges support by the BMBF

Verbundforschung under the grant 05A17STA. The Jülich LOFAR Long Term Archive and the German LOFAR network are both coordinated and operated by the Jülich Supercomputing Centre (JSC), and computing resources on the supercomputer JUWELS at JSC were provided by the Gauss Centre for supercomputing e.V. (grant CHTB00) through the John von Neumann Institute for Computing (NIC). AB and RJvW acknowledges support from the VIDI research programme with project number 639.042.729, which is financed by the Netherlands Organisation for Scientific Research (NWO). MB acknowledges support from the ERC-Stg DRANOEL, no 714245. GDG acknowledges the support from the ERC Starting Grant ClusterWeb 804208. WLW acknowledges support from the CAS-NWO programme for radio astronomy with project number 629.001.024, which is financed by the Netherlands Organisation for Scientific Research (NWO). The scientific results reported in this article are based in part on observations made by the Chandra X-ray Observatory and in part by XMM-Newton, an ESA science mission with instruments and contributions directly funded by ESA Member States and NASA. This research made use of APLpy, an open-source plotting package for Python hosted at <http://aplpy.github.com>.



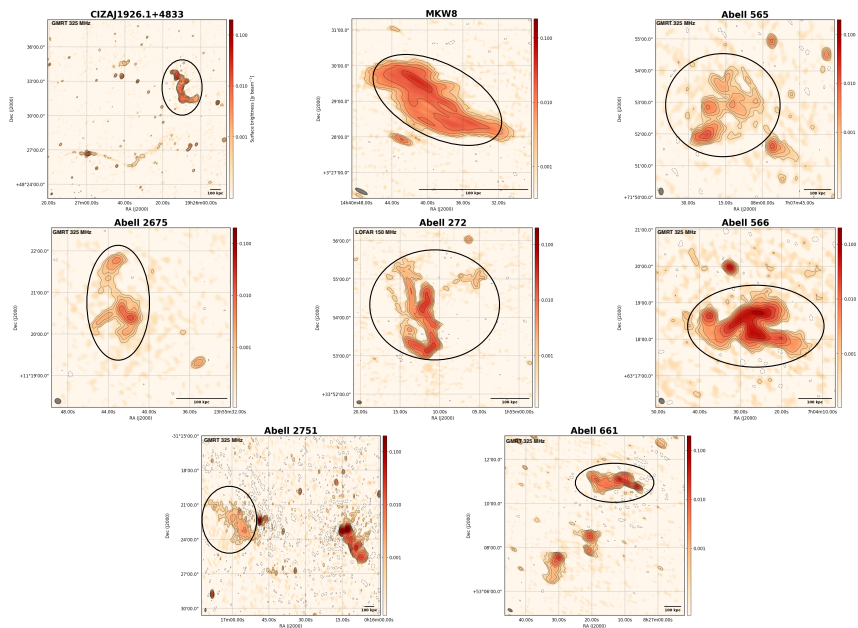
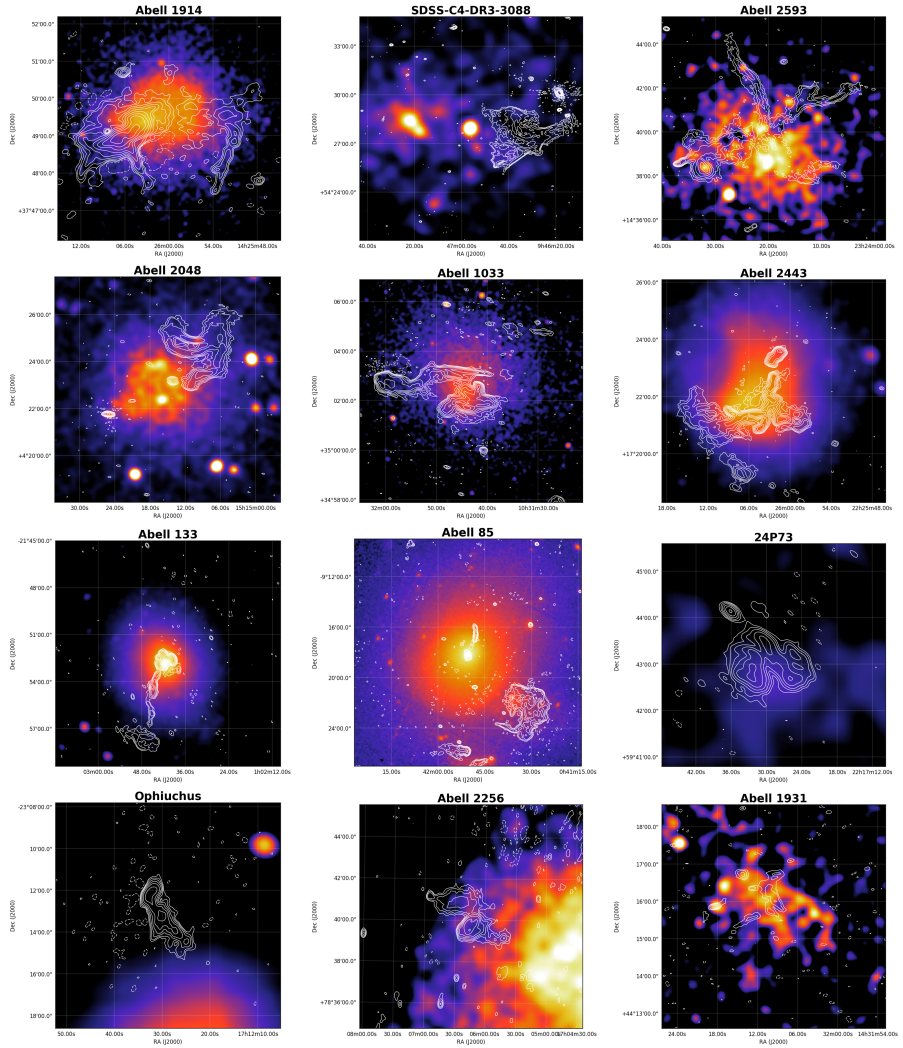


Figure 4.3: Full-resolution radio (LOFAR 150 MHz / GMRT 325 MHz/ GMRT 610 MHz) images of the radio phoenixes. The black ellipses are marked to visualise the candidate radio phoenix. In each of the radio images, the black contours and dashed lines show the $(1, 2, 4, \dots) \times 5 \times \sigma_{\text{radio}}$ and $-3 \times \sigma_{\text{radio}}$ levels, respectively. σ_{radio} is the measured rms noise in the respective radio maps. The beam size is labelled in every image at the bottom left corner.



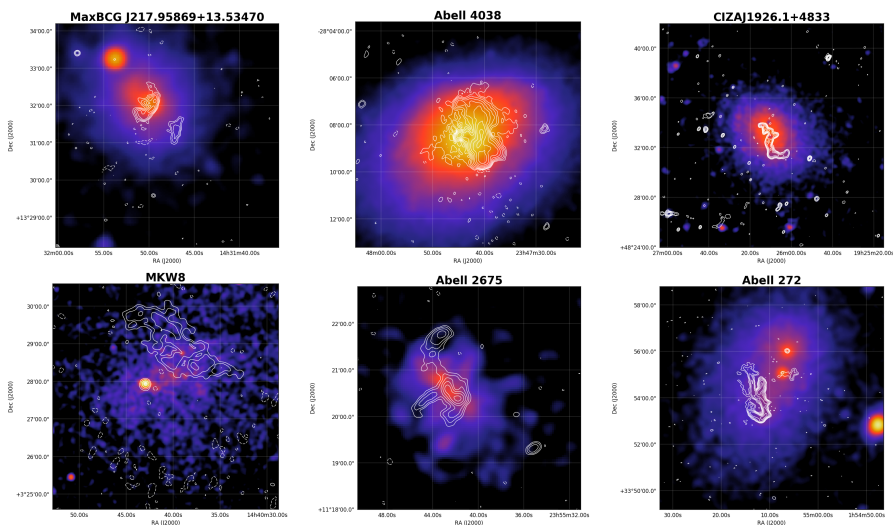
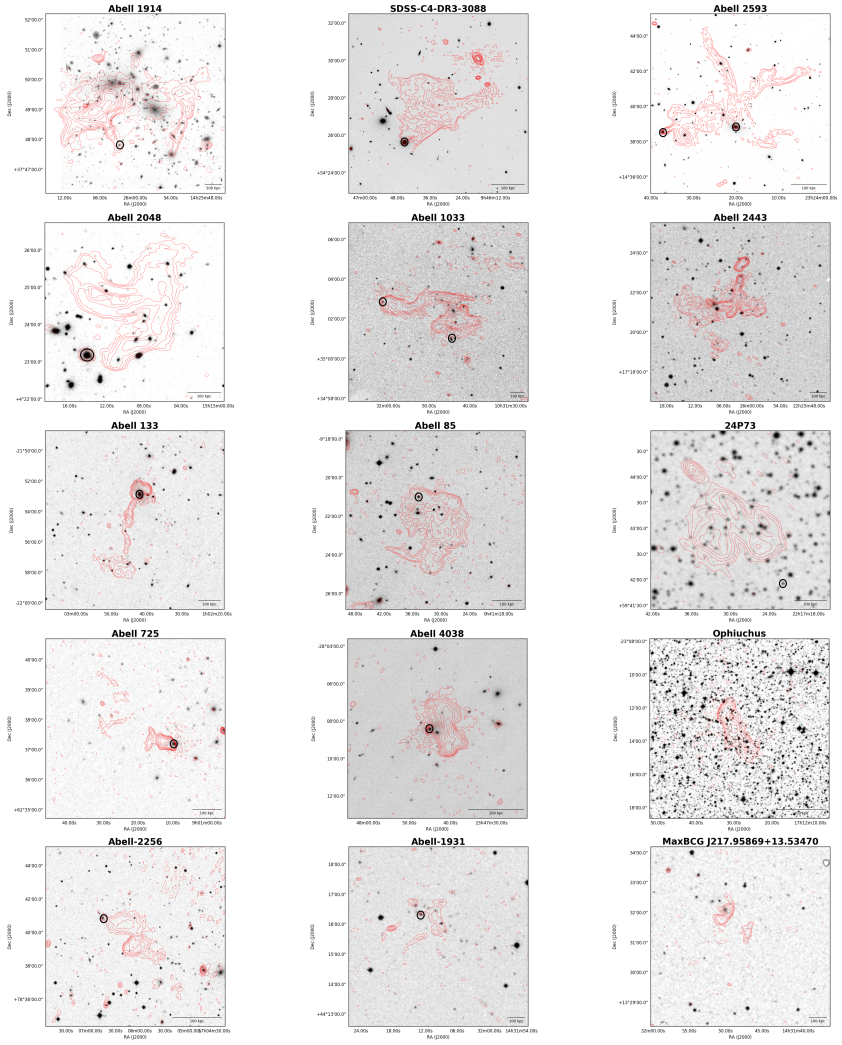


Figure 4.3: Full-resolution radio (LOFAR 150 MHz / GMRT 325 MHz / GMRT 610 MHz) image contours (white; as shown in the Figure 4.3) of all the radio phenices, overlaid on exposure-corrected *Chandra* or *XMM-Newton* images in the 0.5-2.0 keV energy band. The observation details are provided in Table 4.2. In the radio image contours, solid and dashed white lines show the $(1,2,4,\dots)\times 5\times \sigma_{\text{radio}}$ and $-3\times \sigma_{\text{radio}}$ levels, respectively where σ_{radio} is the local rms noise in the radio images.



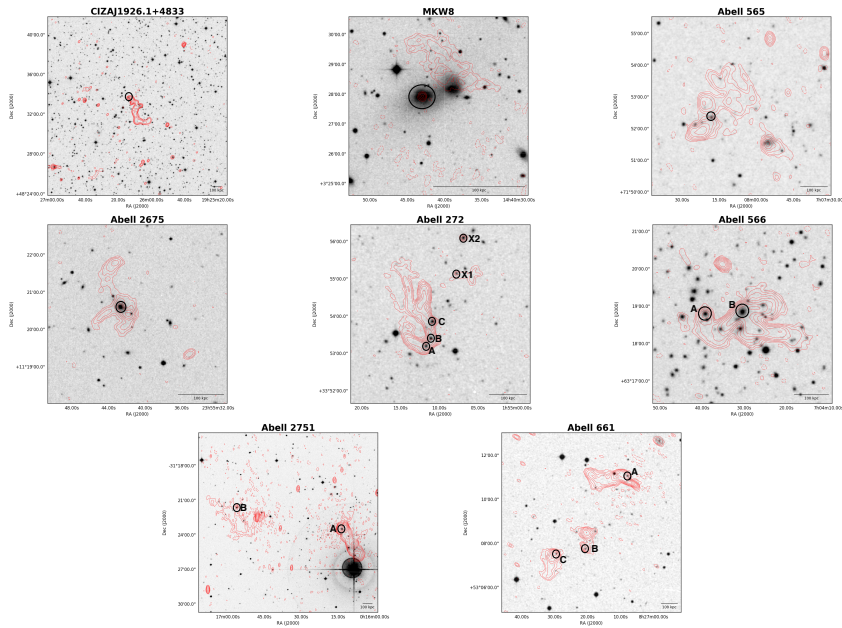


Figure 4.4: Full-resolution radio (LOFAR 150 MHz / GMRT 325 MHz / GMRT 610 MHz) image contours (red; as shown in the Figure 4.3) of all the radio phoenixes, overlaid on DSS r-band optical images. In the radio image contours, solid and dashed red lines show the $(1, 2, 4, \dots) \times 5 \times \sigma_{\text{radio}}$ and $-3 \times \sigma_{\text{radio}}$ levels, respectively, where σ_{radio} is the local rms noise in the radio images.

4.A GMRT Maps

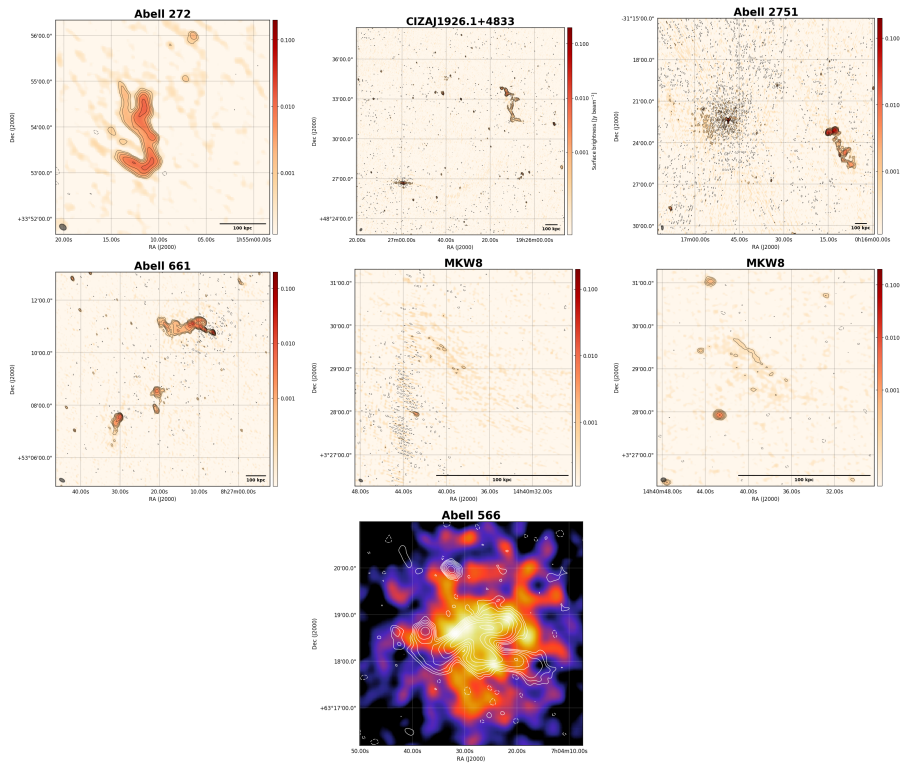


Figure 4.5: Additional radio and X-ray images. Top row (left to right): Abell 272 (GMRT 325 MHz); CIZAJ1926.1+4833 (GMRT 610 MHz); Abell 2751 (GMRT 610 MHz). Middle row (left to right): Abell 661 (GMRT 610 MHz); MKW8 (GMRT 610 MHz) and MKW8 (VLA 1.4 GHz). Bottom row: Abell 566 Suzaku image.

Table 4.5: Total flux density measurements of candidate radio phenices at 150, 325 and 1400 MHz

Sources (Jy)	150 MHz (Jy)	325 MHz (Jy)	1400 MHz (Jy)
Abell 1914	4.68±0.46	0.83±0.08	0.040±0.002
SDSS-C4-DR3-3088	1.83±0.18	0.45±0.05	0.021±0.002
Abell 2593	3.57±0.36	1.45±0.15	0.290±0.012
Abell 2048	1.57±0.25	0.55±0.06	0.019±0.004
Abell 1033	1.30±0.01	0.46±0.05	0.046±0.001
Abell 2443	3.65±0.4	0.41±0.07	0.007±0.0006
Abell 133	10.9±1.2	4.19±0.42	0.210±0.024
Abell 85	8.33±0.7	2.86±0.30	0.042±0.003
24P73	1.40±0.01	0.41±0.04	0.012±0.003
Ophiuchus	6.38±0.32	2.60±0.13	0.630±0.032
Abell 2256	0.57±0.06	0.34±0.03	0.020±0.001
Abell 1931	0.04±0.008	0.004±0.0008	0.0005±0.001
MaxBCG J217.95869+13.53470	0.14±0.01	0.06±0.01	0.001±0.0005
Abell 725	0.75±0.08	0.39±0.04	0.110±0.006
Abell 4038	4.30±0.5	1.40±0.15	0.060±0.003
Abell 13	2.80±0.6	0.63±0.10	0.030±0.002
Abell S753	10.1±0.04	8.50±0.00	0.460±0.0
CIZAJ1926.1+4833	1.15±0.01	0.33±0.03	0.011±0.001
MKW8	1.12±0.11	0.27±0.03	0.002±0.0002
Abell 565	0.27±0.03	0.10±0.01	0.005±0.0003
Abell 2675	0.26±0.03	0.10±0.01	0.008±0.0004
Abell 272	0.75±0.08	0.21±0.02	0.006±0.0003
Abell 566	6.61±0.7	1.54±0.20	0.052±0.001
Abell 2751	0.31±0.03	0.17±0.02	0.024±0.001
Abell 661	0.42±0.04	0.26±0.03	0.055±0.001

